Journal of Geophysical Research: Oceans

RESEARCH ARTICLE
10.1002/2018JC013784

Special Section:
Sea State and Boundary Layer Physics of the Emerging Arctic Ocean

Wave Attenuation Through an Arctic Marginal Ice Zone on 12 October 2015: 2. Numerical Modeling of Waves and Associated Ice Breakup

Fabrice Ardhuin[1], Guillaume Boutin[1], Justin Stopa[1], Fanny Girard-Ardhuin[1], Christian Melsheimer[2], Jim Thomson[3], Alison Kohout[4], Martin Doble[5], and Peter Wadhams[6]

[1]Univ. Brest, CNRS, IRD, Ifremer, Laboratoire d'Océanographie Physique et Spatiale, IUEM, Brest, France, [2]Institute of Environmental Physics, University of Bremen, Bremen, Germany, [3]Applied Physics Laboratory, University of Washington, Seattle, Washington, USA, [4]National Institute of Water and Atmospheric Research, Christchurch, New Zealand, [5]PolarScientific Ltd., Appin, UK, [6]Cambridge Polar Consultants Ltd., Cambridge, UK

Abstract Many processes that affect ocean surface gravity waves in sea ice give rise to attenuation rates that vary with both wave frequency and amplitude. Here we particularly test the possible effects of basal friction, scattering by ice floes, and dissipation in the ice layer due to dislocations, and ice breakup by the waves. The possible influence of these processes is evaluated in the marginal ice zone of the Beaufort Sea, where extensive wave measurements were performed. The wave data includes in situ measurements and the first kilometer-scale map of wave heights provided by Sentinel-1 SAR imagery on 12 October 2015, up to 400 km into the ice. We find that viscous friction at the base of an ice layer gives a dissipation rate that may be too large near the ice edge, where ice is mostly in the form of pancakes. Further into the ice, where larger floes are present, basal friction is not sufficient to account for the observed attenuation. In both regions, the observed narrow directional wave spectra are consistent with a parameterization that gives a weak effect of wave scattering by ice floes. For this particular event, with a dominant wave period around 10 s, we propose that wave attenuation is caused by ice flexure combined with basal friction that is reduced when the ice layer is not continuous. This combination gives realistic wave heights, associated with a 100–200 km wide region over which the ice is broken by waves, as observed in SAR imagery.

Key Points:
- Dissipative mechanisms are dominant for thin ice and periods around 10 s
- Molecular viscosity for basal friction under a continuous ice layer is too strong near the ice edge
- Ice breakup and wave attenuation are well reproduced with a realistic combination of basal friction and flexural dissipation

Correspondence to:
F. Ardhuin,
ardhuin@univ-brest.fr

Citation:
Ardhuin, F., Boutin, G., Stopa, J., Girard-Ardhuin, F., Melsheimer, C., Thomson, J., et al. (2018). Wave attenuation through an arctic marginal ice zone on 12 October 2015: 2. Numerical modeling of waves and associated ice breakup. *Journal of Geophysical Research: Oceans*, *123*. https://doi.org/10.1002/2018JC013784

Received 12 JAN 2018
Accepted 21 MAR 2018
Accepted article online 26 MAR 2018

1. Introduction

Wind-generated ocean waves are a key component in air-sea interactions. On some occasions, waves have been observed to propagate hundreds of kilometers into sea ice (Liu & Mollo-Christensen, 1988; Wadhams & Doble, 2009). The attenuation of ocean waves penetrating in ice-covered regions is important for navigation and it also has important geophysical consequences. In particular, higher waves are more capable of breaking the ice (Kohout et al., 2014), thereby enhancing air-sea fluxes. Also, the wave momentum lost where waves dissipate is a force pushing on the ice cover (Masson, 1991; Stopa et al. 2018). The goal of the present paper is to contribute to the quantitative understanding of wave attenuation and how it depends on ice properties, using unique remote sensing data and recently developed parameterizations in numerical wave models.

The physical processes and magnitude of the attenuation rate are poorly known and a wide range of parameterizations have been proposed in spectral wave models (e.g., Mosig et al., 2015; Liu & Mollo-Christensen, 1988; Squire et al., 1995; Stopa et al., 2016; Wadhams, 1973; Williams et al., 2013). Progress has been limited by the availability of data for wind, ice and waves, and the complexity of different ice types and their varying mechanical properties within the marginal ice zone (MIZ).

Several recent studies have reported interesting behaviors of waves in ice, close to the ice edge (Collins et al., 2015; Doble & Bidlot, 2013; Kohout et al., 2014; Sutherland & Gascard, 2016), or all the way to the middle of the Arctic (Ardhuin et al., 2016). Unfortunately, these experiments generally lacked spatial coverage to resolve the evolution of the wave field, or some measurements, in particular ice properties. Older extensive experiments such as MIZEX (Wadhams et al., 1986) revealed properties of wave evolution near the ice edge. Recent experiments such as N-ICE can be combined with satellite remote sensing data to obtain a large scale view of wave evolution and ice properties (Itkin et al., 2017).

Here we use both remote sensing and in situ wave data from the Sea State 2015 experiment (Thomson et al., 2017, 2018), which covered the freeze-up of the Beaufort Sea over the month of October 2015. We particularly focus on the "Wave Array 3" deployment on 11–13 October that was marked by a strong storm with wind speeds from the east exceeding 15 m/s, as measured from the R/V Sikuliaq, and wave heights up to 4.5 m (as detailed below). This storm led to ice melting over 100 km, as illustrated in Figure 1, with twice daily ice concentration maps estimated from the AMSR2 satellite radiometer, using the Artist Sea Ice algorithm (Kaleschke et al., 2001; Spreen et al., 2008).

Most of the wave buoys were deployed within 20 km of the ice edge in regions dominated by frazil, grease, or pancake ice. From these buoy data, this event has been studied in detail by Rogers et al. (2016) and Cheng et al. (2017), with particular adjustment of wave dissipation parameterizations in pancake ice. In particular, Cheng et al. (2017) found that the dispersion relation deviated by less than 5% from the linear wave dispersion without ice for frequencies under 0.2 Hz. We will thus use the ice-free dispersion relation in the present paper.

Here we focus on wave propagation deeper into the ice thanks to a novel measurement of wave spectra in the ice from remote sensing data, detailed in Part 1 (Stopa et al. 2018). Indeed, Sentinel-1A (S1A) synthetic aperture radar (SAR) imagery was acquired in Interferometry Wide swath (IW) mode around 16:50 UTC on 12 October. This mode allows a direct mapping of wave orbital velocities in the ice thanks to a relatively high resolution around 10 m (Ardhuin et al., 2015, 2017a). The S1A IW image covers 400 km in range (across the swath), and over 1,000 km in azimuth (along the satellite track), with a location indicated in Figure 1. The map of wave heights is reproduced in Figure 2a, with data of doubtful quality removed in Figure 2b.

The observed wave pattern may be influenced by dissipation and scattering processes. Here we will particularly evaluate parameterizations for the effects of basal friction, scattering by ice floes, and dissipation due to ice flexure. All of these take into account a maximum floe size diameter D_{max} which is itself determined from the interactions of waves with a continuous layer of ice. These processes are a priori very different from those dominant in grease, frazil, or pancake ice (e.g., de Carolis et al., 2005; Rogers et al., 2016; Zhao & Shen, 2015). Because the present data set contains all ice types, our approach will be to evaluate and adapt a model developed for a single layer of ice possibly broken into flows.

The "out of the box" model setup that will be our reference run was adjusted to give reasonable wave heights around Antarctic sea ice in 0.5° resolution model. This default model run gives a snapshot of wave heights, directions, and maximum floe sizes that is shown in Figure 2c. The model setup is described in section 2, including a summary of the main features of the parameterizations presented by Boutin et al. (2018). Variations in model forcing and settings are investigated in section 3, giving plausible explanations for the observed wave decay. Discussion and conclusions follow in sections 4 and 5, respectively.

2. Numerical Wave Model and Results

2.1. General Model Principles

In this paper, we will not take into account ocean currents because of limited information for this region. We note that Pickart (2004) mentions a mean shelf break jet with velocities of the order of 10 cm/s. However, strong mesoscale or submesoscale eddies at the ice edge have been found with velocities up to 1 m/s (Lund et al., 2018). Similar features have been reproduced in numerical simulations by Manucharyan and Thompson (2018). Their interaction with ocean waves and sea ice, although possibly important, will not be considered here.

We use a phase-averaged spectral representation of the wave field, in which the surface elevation variance is distributed across frequencies f and directions θ with the directional wave spectrum $E(f, \theta)$. Once currents are neglected and considering waves in deep water, the evolution of the wave spectrum follows the energy balance equation (e.g., Ardhuin et al., 2010; Gelci et al., 1957; WAMDI Group, 1988),

$$\frac{\mathrm{d}E(x,y,f,\theta,t)}{\mathrm{d}t} = [a_{\mathrm{atm}}S_{\mathrm{atm}} + a_{\mathrm{nl}}S_{\mathrm{nl}} + a_{\mathrm{oc}}S_{\mathrm{oc}}] + a_{\mathrm{ice}}S_{\mathrm{ice}}, \quad (1)$$

in which the Lagrangian derivative on the left-hand side follows a wave packet in physical (x, y) and spectral (f, θ) coordinates. The right-hand side is the sum of all source terms S_i, which is the rate of change of the

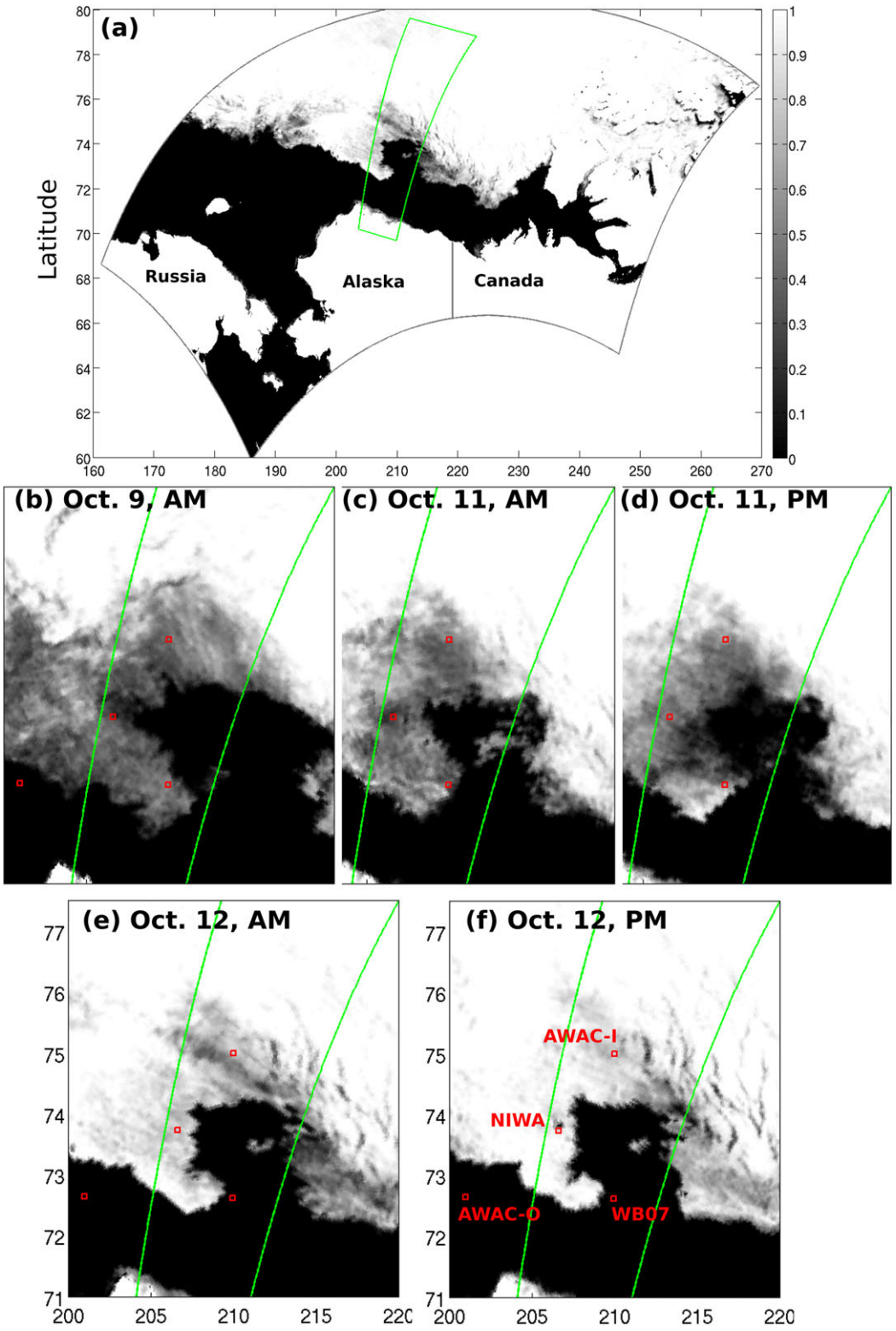

Figure 1. Sea ice concentration inferred from the AMSR2 radiometer using the ASI algorithm. (a) General situation in the Beaufort Sea from 0 to 12 AM UTC on 12 October. Ice concentrations are only shown in the model domain used in this study, and the green box is the region sampled by Sentinel-1A SAR at 5 PM on 12 October. (b)–(f) The evolving sea ice concentration. Red squares mark the location of in situ sensors, with their positions at 5 PM on 12 October. The labels "AM" or "PM" means that passes from the morning or evening have been used.

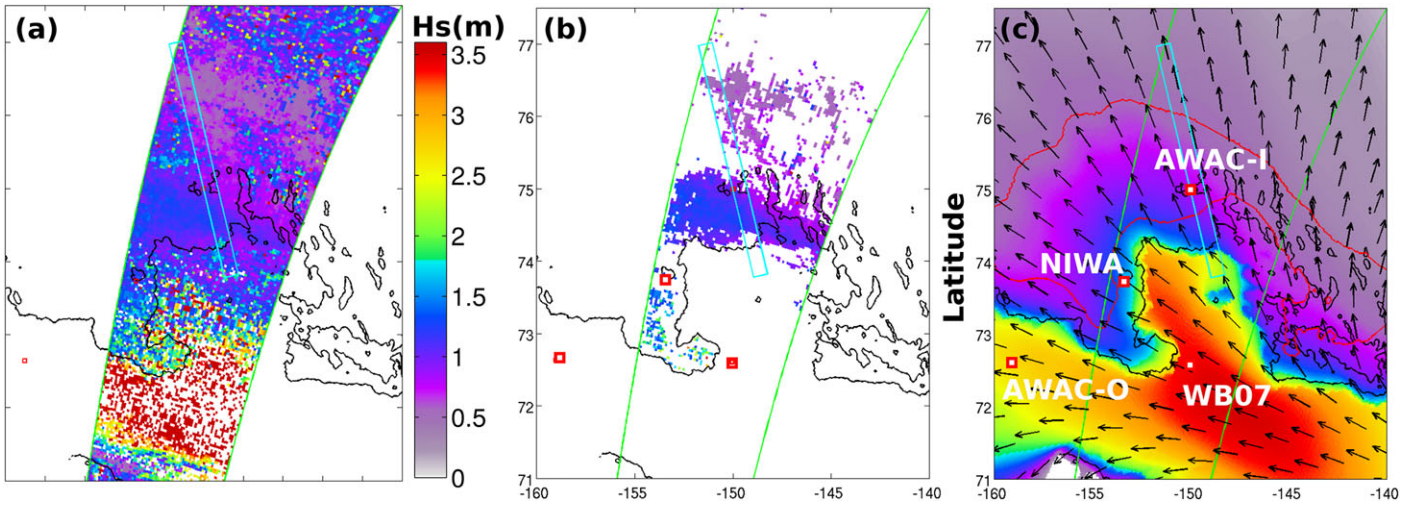

Figure 2. Observed and modeled wave heights in the Beaufort Sea on 12 October 2015 at 17:00 UTC. (a) Full map of wave heights derived from an S1A IW image including data corrupted by ice features and nonlinear SAR effects, (b) S1A data expected to be of good quality in terms of wave spectrum, based on subimage homogeneity and azimuthal cut-off (see Part 1 for details). (c) The modeled map shows H_s in colors, with the black line indicating the 70% ice concentration contour, derived from AMSR2, and the red lines show the 50 and 75 m contours of D_{max}. The green lines mark the edges of the S1A swath observed on that day. In all three plots, the locations of in situ instruments are indicated by white or red squares. The cyan transect identifies the region where the wave properties are analyzed in more detail.

elevation spectral density, with a scaling a_i that is a function of the ice properties. The different source terms represent the contribution of different processes to the spectrum evolution, S_{atm} corresponds to interactions with the atmosphere, including wave generation by the wind and wind generation by swells, S_{nl} is an internal redistribution of wave energy between different wave components due to nonlinear interactions, and S_{oc} is a the (usually negative) source of wave energy to the upper ocean, generally dominated by wave breaking.

2.2. Model Setup

In order to use the full resolution AMSR2 forcing for sea ice concentration c_i, we have chosen a model grid that exactly matches the 3 km resolution of the c_i maps produced by the University of Bremen (Spreen et al., 2008). We have restricted this polar-stereographic grid to the Beaufort and Chukchi seas, including Bering Straits, as shown in Figure 1a. This grid uses the curvilinear grid capability developed by Rogers and Campbell (2009). We use the WAVEWATCH III model version 6.04, which slightly differs from version 5.16 described by The WAVEWATCH III® Development Group (2016). These differences include adjustments of the IC2 and IS2 wave-ice interaction parameterizations as described by Boutin et al. (2018) and in the section 3 of the present paper. Our spectral grid uses 24 directions and 32 frequencies exponentially spaced from 0.0373 to 0.73 Hz. Equation (1) is solved with a splitting method, with a global time step of 300 s, an advection and refraction steps of 75 s, and a minimum source term time step of 1 s. In order to properly integrate the source terms across the ice edge, the S_{ice} source term is integrated separately with an implicit method.

2.3. Choice of Parameterizations

In the present work, we use the parameterizations by Ardhuin et al. (2010) as revised in Rascle and Ardhuin (2013) and The WAVEWATCH III® Development Group (2016) for S_{atm} and S_{oc}, and for S_{nl} we use the Discrete Interaction Approximation of Hasselmann and Hasselmann (1985). In the WAVEWATCH III model, these are activated by the ST4 and NL1 options, using default values for the parameters, except for those mentioned in Table 1.

The wave-ice interaction source term S_{ice} is further separated into scattering, basal friction, flexural dissipation, and viscoelastic dissipation

$$S_{ice} = S_{isc} + S_{ibf} + S_{ifl} + S_{ive}. \quad (2)$$

All these terms are scaled by the ice concentration c_i, namely $a_{ice} = c_i$, and $a_{atm} = a_{oc} = (1 - c_i)$, and $a_{nl} = 1$. This particular choice follows Rogers et al. (2016) and may underestimate a possible wind-wave growth over ice.

Table 1
Names of Model Runs and Corresponding Model Parameters

Name	β_{max}	H_i (m)	C_{isc}	C_{ibf}	B_{ine} (N m^2 s$^{1/3}$)	r_D	σ_c (MPa)
REF	1.6	0.15	1	1	3×10^7	0	0.274
ZER	1.6	0.15	**0**	**0**	**0**	0	0.274
IBF ONLY	1.6	0.15	**0**	1	**0**	0	0.274
H30	1.6	**0.30**	1	1	3×10^7	0	0.274
STRONG	1.6	0.15	1	1	3×10^7	0	**0.6**
DBF	1.6	0.15	1	1	$\mathbf{3 \times 10^7}$	0.3	**0.274**
DINE+	1.6	0.15	1	1	$\mathbf{1 \times 10^7}$	0.3	**0.274**
REF2	1.6	0.15	1	1	2×10^7	0.3	0.6
REF2H30	1.6	**0.30**	1	1	2×10^7	0.3	0.6

Note. Simulations in which the basal friction is reduced for finite floe sizes are in the lower half of the table, with $r_D > 0$, these are discussed in section 3. The parameters that we varied are the ice thickness H_i which is taken uniform, the scattering and basal friction coefficients coefficient C_{isc} and C_{ibf}, the inelastic flow law parameter B_{ine}, the floe size effect on basal friction r_D, and the ice flexural strength σ_c. Parameters that are different from the REF or REF2 settings are highlighted in bold.

In practice, the viscoelastic dissipation term S_{ive} has been developed for grease, frazil, or pancake ice (e.g., Cheng et al., 2017; Rogers et al., 2016), which do not have a single ice layer floating on the water. This term represents all dissipation effects in the layer where ice and water are present (viscous dissipation, collisions, friction between ice pieces, etc.). In the present work, we will use $S_{ive} = 0$. The other three terms are designed to apply to a single layer of ice which may be fragmented (in the horizontal dimension) into floes, as illustrated in Figure 3. The scattering parameterization follows the approach of Kohout and Meylan (2008) and Williams et al. (2013), with reflection coefficients at ice-water interfaces estimated from the normal reflection at the straight boundary of a semi-infinite ice sheet. The scattering of a single interface is multiplied by the number of interfaces per unit area, which is inferred from the maximum floe size D_{max} and an assumed power law for the floe size distribution. An important difference introduced by Boutin et al. (2018) is that the scattered wave energy is redistributed in other directions to enforce energy conservation.

The determination of D_{max} follows Williams et al. (2013), with an adaptation for random waves using a partial integration of the wave spectrum with a moving window in frequency that gives different ice breakup possibilities for different wave frequencies. The value of D_{max} is computed at each time step from the local wave field. This gives two unrealistic effects that require a coupled ice-wave model to correct: D_{max} is not advected with the ice drift, and D_{max} automatically increases when the wave height goes down. For our case of an active storm, and over only a few hours, we expect that these effects are not too important.

Basal friction was generalized for random waves with a possible laminar to turbulent boundary layer below the ice, using the laminar theory by Liu and Mollo-Christensen (1988), and the turbulent bottom boundary

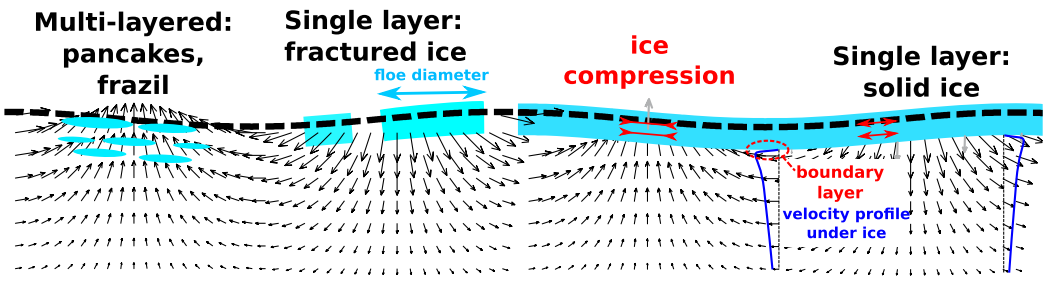

Figure 3. Schematic of ice types and associated processes that influence ocean waves. The black arrows represent a snapshot of the flow in the water. Ice is represented by light blue areas, and the thick dashed line represents the position of the free surface in the absence of ice. Basal friction is due to the strong shear in the boundary layer at the base of the ice layer. Inelastic dissipation occurs within the ice layer due to grain dislocations. Pancakes tend to clump together due to horizontal convergence in the water, and dissipation may occur by a variety of friction processes involving ice and water, all of those can be parameterized by a viscoelastic model.

layer theory by Grant and Madsen (1979) generalized to random waves by Madsen (1994). For the turbulent case, the flow and dissipation rate are fully determined by the under-ice roughness length which is here taken constant at 0.1 mm, similar to medium-grained sand.

Finally the inelastic dissipation proposed by Boutin et al. (2018) is loosely based on the stress-strain relations measured by Cole and Durell (2001) at a frequency of 0.1 Hz. These show a nonlinear relation that was attributed to dislocations and that can be modeled by a flow law similar to the one proposed by Nye (1953) for glaciers

$$\left(\frac{d\varepsilon}{dt}\right)_{ij} = \frac{\tau^{n-1}}{B_{\text{ine}}^{n}}\sigma'_{i,j}, \tag{3}$$

where $\varepsilon_{i,j}$ is the strain tensor, $\sigma'_{i,j}$ is the deviatoric stress tensor, τ is the shear stress equal to $|\frac{1}{2}\sigma'_{ij}\sigma'_{ij}|^{\frac{1}{2}}$, and B_{ine} is the flow law constant, which is a function of ice temperature. The flow parameter B_{ine} would be the inverse of a viscosity for $n = 1$, and the dissipation increases when B_{ine} decreases. Here we use $n = 3$, for which Boutin et al. (2018) used $B_{\text{ine}} = 10^7$ N m^{-2}s$^{1/3}$, which is of the order of magnitude found by Wadhams (1973).

2.4. Wind and Sea Ice Conditions

2.4.1. Wind

Numerical wave models in the open ocean are known to be very sensitive to errors in wind speed and direction (e.g., Rascle & Ardhuin, 2013). Here we combine ECMWF operational analyses and forecasts into hourly wind fields. In our region of interest, around the WB07 buoy, this ECMWF wind has a maximum easterly wind of 14.5 m s^{-1} on 12 October at 14:00 UTC, and values above 13 m s^{-1} for most of the day. These value are lower than what was measured on R/V Sikuliaq which exceeded 15 m s^{-1}. This may be due to poorly resolved low level wind jets near the ice edge (Guest et al., 2018). We compensated for this effect by increasing the $\beta_{\max}$ wind-wave growth parameter from 1.45, which is our default value for global-scale applications, to 1.6. As shown in Figure 4, this adjustment brings the wave height and wave spectrum shape at the off-ice buoy WB07 in close agreement with the measurements. Waves are also well reproduced at the other off-ice instrument AWAC-O.

A striking result in Figure 4 is the very strong underestimation of wave energy at the NIWA buoy. This can be attributed to our choice of ice forcing. Indeed, sea ice can have such a large impact on waves, with exponential attenuation on scales of the order of 10 km (e.g., Liu et al., 1991; Rogers et al., 2016), that it is also most important to specify the ice properties used to force the wave models. In our case, sea ice is characterized by three parameters that may vary with horizontal position (x, y): ice concentration c_i, average thickness H_i, and maximum floe size diameter $D_{\max}$, but that last parameter is computed from H_i and the wave properties.

2.4.2. Sea Ice Concentration

As shown in Part 1, the position of the ice edge could be estimated from SAR imagery using the normalized variance of the radar backscatter. However, because our model requires ice information over the entire model grid (even outside of the S1A SAR image) we chose to force the wave model with data derived from the AMRS2 radiometer using the ASI algorithm (Kaleschke et al., 2001; Spreen et al., 2008). This gives a 3 km resolution ice concentration field which is produced with a daily time step at the University of Bremen. Given that the ice moves very fast in this season, the raw AMSR2 data were reanalyzed to produce 12 hourly maps that gather all the AMSR2 passes acquired between 00:00 and 13:59 UTC, and 10:00 and 23:59 UTC for the morning (AM) and evening (PM) fields, respectively. The overlap in time allows a full coverage of the Arctic. Note that within the AM and PM passes, later passes are given precedence over earlier passes.

Since the WAVEWATCH III model updates the ice in the middle of the forcing interval, we set the time stamp to 00:00 for AM and 12:00 for PM, so that the ice field "jumps" to the AM field at 06:00 and to the PM field at 18:00. As a result, the 17:00 model output on 12 October corresponds to the AM field. The AMSR2 data were actually acquired around 11:00 (AM passes) and 19:00 (PM passes).

Both AM and PM fields are very similar for 12 October in our region of interest (Figures 1e and 1f). We thus expect that this time-discontinuous treatment of the ice forcing has a limited impact on the model result.

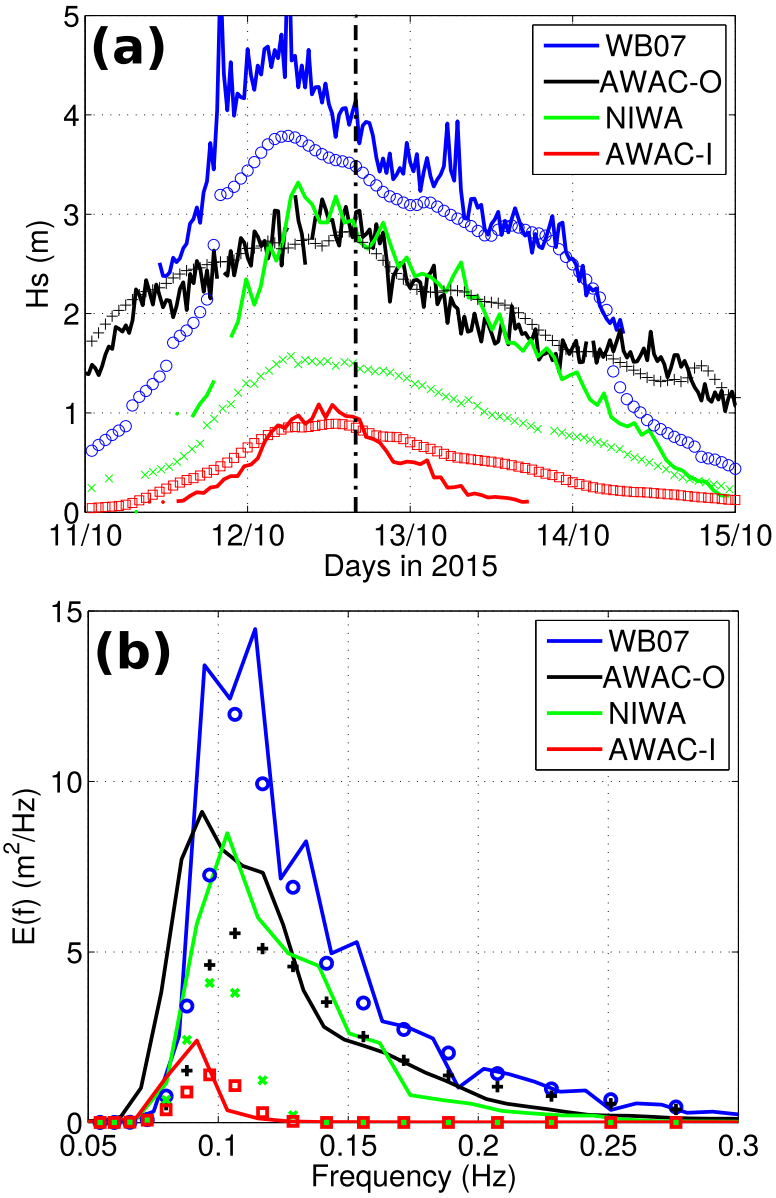

Figure 4. (a) Time series of measured (solid lines) and modeled (symbols) H_s. See Figure 2a for the locations of the in situ sensors at the time of the S1A acquisition, marked by the vertical dash-dotted line. (b) Observed and modeled surface elevation spectra at 16:30 on 12 October.

Despite its high spatial resolution, the c_i maps are not perfect. A particular problem is the definition of ice concentrations in the region between the NIWA and WB07 buoys. Indeed, ship-based observations show that the concentrations around 0.5 in Figure 1b between the WB07 and NIWA buoys correspond to pancake ice with bands of open water that become broader on 12 October.

Other qualitative information on the ice is provided by radar backscatter information shown in Figure 5a. This shows the C-band Advanced SCATterometer (ASCAT) daily roughness map produced by Ifremer at 12.5 km resolution following similar products using the ERS-1/2 scatterometer (Gohin & Cavanié, 1994). This data clearly show the absence of multiyear ice in the entire S1A image. There is also a detection of ice (blue shading) to the east of the NIWA buoy. The SAR imagery gives higher resolution details (Figures 5b–5e). As discussed in Part 1, there are finger-like features 500 m to 2 km wide, oriented in the wave propagation direction, in the region of the NIWA buoy, with intermediate radar backscatter level and less pronounced wave features (for example, in box 1 Figure 5c). Based on the ship observation these are open water

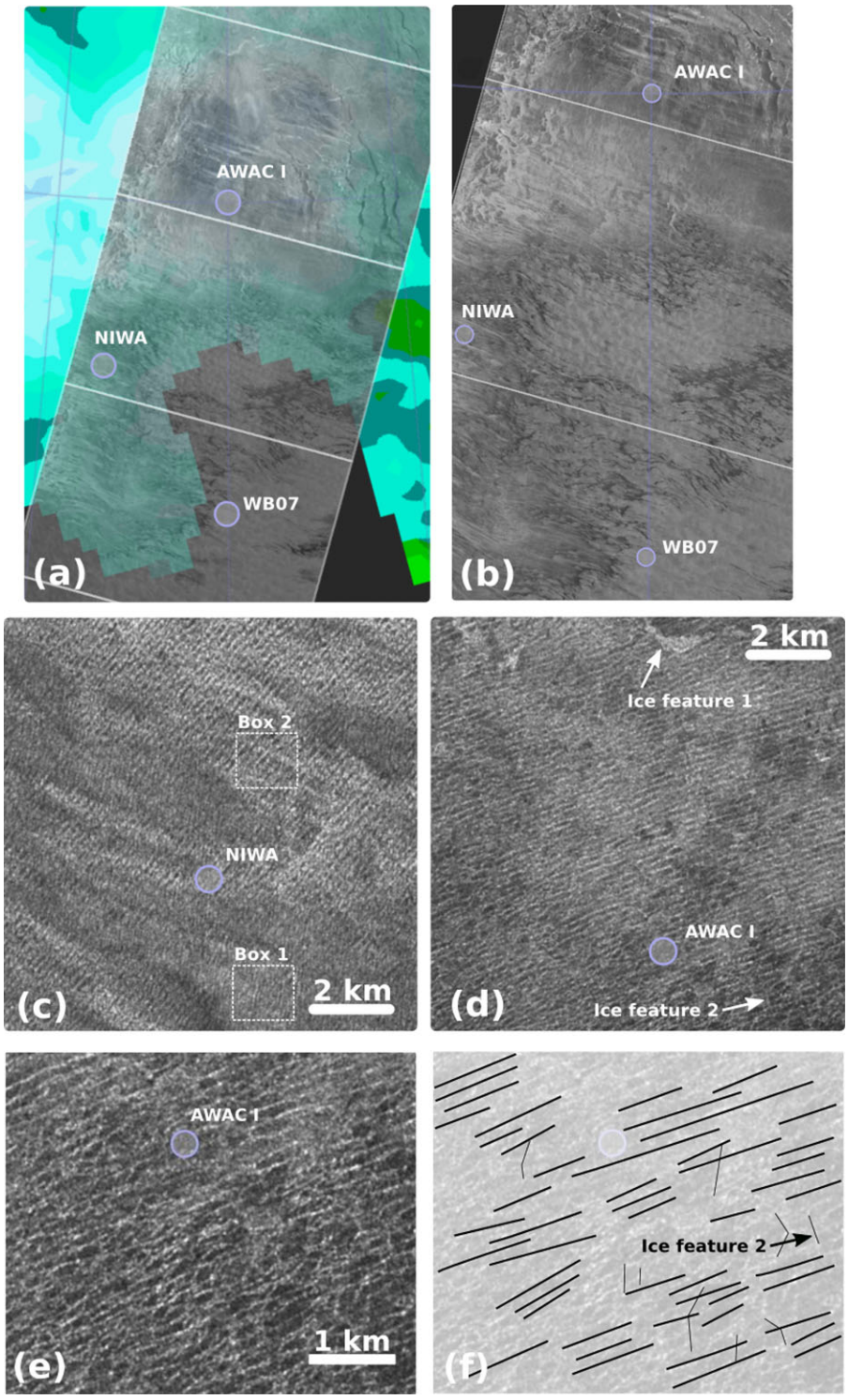

Figure 5. Qualitative information of ice properties. (a) In colors, ASCAT surface roughness map showing the absence of multiyear ice in the area. (b) Radar backscatter from the S1A IW image, (c and d) close-up of SAR image around the NIWA buoy and the AWAC-I. (e) Detail at full resolution showing possible ice features around AWAC-I. (f) Possible interpretation of Figure 5e with wave crests as thick lines and ice features as thin lines. A full resolution image can be visualized interactively at http://tiny.cc/S1AOct12.

regions, and they are interleaved between bands of pancakes such as around box 1, in which the wave patterns have different directions and appear more pronounced. As a result, even if the NIWA buoy is in more than 70% ice according to the ASI processing of AMSR2, the SAR image puts in on the edge of a band of open water. We thus interpret the strong wave height underestimation by the model in Figure 4a as an error in the model forcing: the AMSR2-derived ice concentration is too high and gives a false impression of a well defined section of the ice edge, oriented north-south and located 40 km to the east of the NIWA buoy. It is known that the ASI algorithm can retrieve too high ice concentration because of weather influence (precipitating clouds), and comparison with the ASI sea ice concentration on the previous and the subsequent days show much lower values and a much less sharp boundary.

The fuzzy nature of the boundary is also confirmed by the SAR image cut-off parameter λ_c (Kerbaol et al., 1998; Stopa et al., 2015, see also Part 1) from which we may estimate the wave orbital velocity

$$w_{\rm rms}=\left(\int_0^\infty (2\pi f)^2 E(f) df\right)^{1/2}. \tag{4}$$

With our incidence angles around 42° at the NIWA buoy, the relationship between λ_c and $w_{\rm rms}$ should also depend on the wave propagation direction, including the unresolved short waves (Kerbaol et al., 1998). For all waves in a single direction θ relative to the range direction θ_r, this is

$$w_{\rm rms}=\frac{\lambda_c H}{\pi V\sqrt{\cos^2(\theta-\theta_r)+\sin^2(\theta-\theta_r)\sin^2(\theta_i)}}, \tag{5}$$

where H is the satellite altitude, V is the satellite velocity, and θ_i in the radar incidence angle which here varies from 30° to 46° across the S1A swath, from east to west. Here, for simplicity we have taken $\theta-\theta_r$=45° to account for a broad field of short waves in the open water, and oblique propagation of a narrower spectrum further into the ice. Results are shown in Figure 6b.

We note that the $w_{\rm rms}$ values are consistent with the model result in the open water. Also $w_{\rm rms}$ has a sharp transition to lower values where the waves cross the ice edge, except around the NIWA buoy, where SAR-derived values of 0.7–0.8 m s^{-1} correspond to the open water bands. These bands are not reproduced in the model due to their absence in the forcing c_i maps derived from AMSR2.

Further from the edge, the SAR-derived $w_{\rm rms}$ does not go below 0.6 m s^{-1}, which is much more than the 0.15 m s^{-1} estimated from the AWAC-I sensor. We hypothesize that there is an overestimation of λ_c in our SAR processing, maybe due to ice features and instrument noise. As a result of this overestimation, the estimation of the wave spectrum may be biased high given the relation between the linear spectrum (in which cut-off effects are not corrected) and the quasi-linear spectrum (see Hasselmann & Hasselmann, 1991, equation (56), see also Part 1). This is most problematic near the ice edge where the short wave blurring effect may be important (Ardhuin et al., 2017b). In the following, we will thus show wave heights estimated from both the linear and the quasi-linear spectrum.

2.4.3. Sea Ice Thickness and Maximum Floe Diameter

The maximum floe diameter $D_{\rm max}$ is initialized with a uniform value $D_{\rm max}$ = 1,000 m, and computed following Williams et al. (2013) and Boutin et al. (2018).

The mean thickness H_i affects both the scattering and inelastic dissipation terms, it may thus have an important effect on wave attenuation, either directly or via its impact on $D_{\rm max}$. Possible sources of data, from models and remote sensing, are discussed by Cheng et al. (2017). In particular, for our relatively thin ice conditions, the L-band SMOS radiometer may provide useful information (Kaleschke et al., 2012). However, as discussed in Part 1, the 5 cm SMOS-derived thickness at the NIWA buoy and 10 cm around AWAC-I appears unrealistically low compared to the in situ observations in the range $0.10 < H_i < 0.45$ m. Still, SMOS gives a realistic general increase in thickness from the ice edge to within the pack. Given the uncertainties on the ice concentration near the edge, we have chosen to simplify our analysis by forcing the model with a constant thickness H_i. The reference model run uses H_i = 0.15 m. Figure 7a shows that a variation from H_i = 0.15 m to H_i = 0.30 m has a moderate 0.1–0.2 m impact on the resulting wave heights. Sensitivity to H_i will be further discussed in section 3.

Figure 7a also shows that the observed wave heights correspond to a large attenuation, compared to a simulation without attenuation. The energy is reduced by a factor 2.5 at 50 km from the ice edge, to about 3 to 4 at

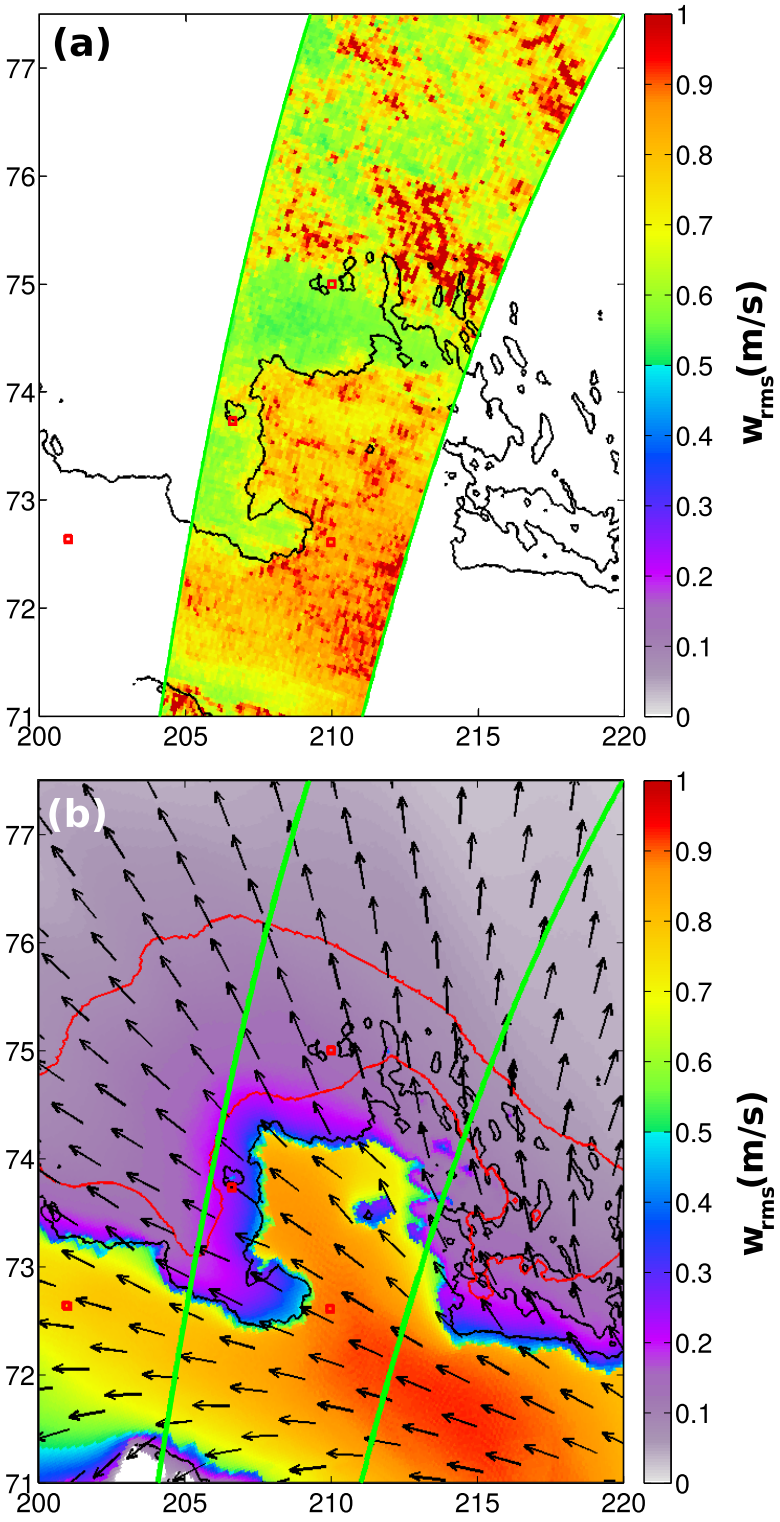

Figure 6. Estimated and modeled surface root mean square velocity w_{rms}. (a) Estimation from the SAR-derived cut-off parameter λ_c, using equation (5), (b) modeled map shows w_{rms} in colors, with the black line indicating the 70% ice concentration contour, derived from AMSR2, and the red lines show the 50 and 75 m contours of D_{max}. The green lines mark the edges of the S1A swath observed on that day. The locations of in situ instruments are indicated by red squares.

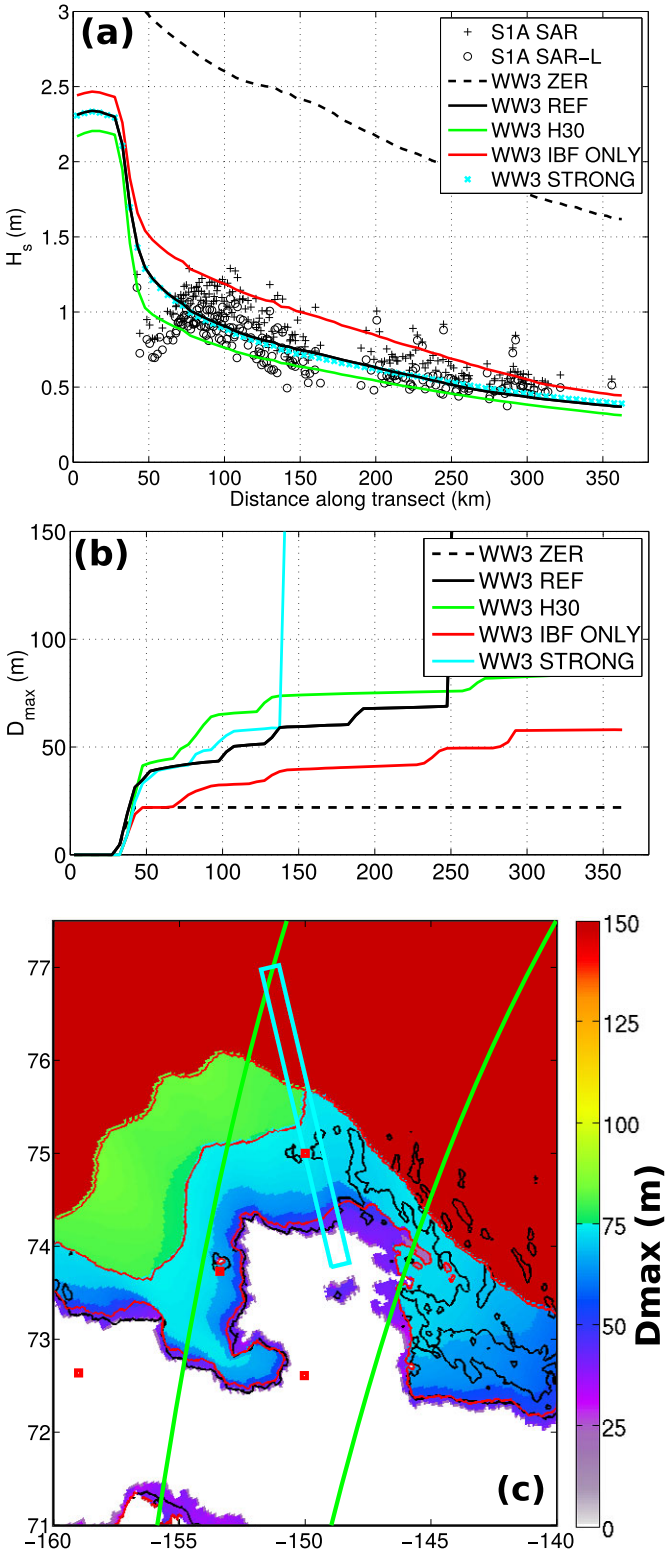

Figure 7. (a) Evolution of H_s along a transect (see Figure 2 for transect position), for the SAR-derived values including (S1A SAR) or not (S1A SAR-L) the correction for the azimuthal cut-off, and several model runs. These include a simulation without dissipation nor scattering (ZER), our reference (REF) model run, and the reference with the ice thickness increased to 30 cm (H30). The model run with only basal friction (IBF ONLY) corresponds to $S_{ice} = S_{ibf}$. (b) Evolution of the modeled maximum floe diameter D_{max} along the transect, (c) map of D_{max} for the REF model run. The AWAC-I instrument is located at $x = 135$ km. The "half broken" ice texture in the SAR image is found between 127 and 145 km.

300 km from the ice edge. In our reference simulation, this attenuation is mostly caused by basal friction, which is why the model result is weakly sensitive to the ice thickness. As a result, the estimation of D_{max} has a limited influence on the wave evolution. We note that the reference simulation gives broken ice as far as 100 km beyond the AWAC-I mooring (Figures 7b and 7c), whereas the SAR image clearly shows leads and kilometer-size floes already 20 km beyond the mooring. The largest floes produced by wave-induced breakup have a diameter that is around 80 m, half of the largest wavelengths of energetic waves.

Many other parameterizations besides basal friction can be adjusted to give similar wave attenuation rates. For example, Rogers et al. (2016) found an attenuation coefficient $2k_i$ for the wave energy that is in the range $2\times10^{-6} < 2k_i < 2\times10^{-5}$ m^{-1} at our dominant frequency around 0.1 Hz. This can be reproduced with a viscoelastic model using a viscosity of 0.03 m^2/s in an ice layer of thickness $H_i = 30$ cm. This attenuation corresponds to half-decay distances $L_{1/2}=\log(2)/(2k_i)$ between 35 and 350 km, of the same order as the effect of molecular viscosity below a rigid plate. In the absence of measurements of the velocity profile across and below the ice layer, it is difficult to decide which process is most important, and both effects could be combined. Such a combination would require a more realistic representation of basal friction in broken ice.

However, our parameterization of basal friction, following Liu and Mollo-Christensen (1988), assumes a continuous solid ice sheet. This is not very realistic for the pancake-covered region near the NIWA buoy, where the pancakes are able to follow some of the horizontal orbital wave motion.

3. A Possible Adjustment of Basal Friction

Floes or pancakes with diameters much shorter than the ocean wave wavelength follow at least partly the horizontal motion. It is thus logical to reduce the relative velocity between the ice and the water from which the dissipation rate is estimated. The difficulty is to quantify this reduction.

3.1. Parameterization

Our goal here is to evaluate the possible impact of a reduction in basal friction due to horizontal motion of ice plates, which is also discussed by Marchenko and Chumakov (2017). Indeed, all the buoys deployed by J. Thomson in pancake ice during this experiment (personal communication, 2018) have a horizontal motion that has the same amplitude as the vertical motion and pancakes are rafted in multiple layers with little resistance to converging and diverging motions. On the contrary some other observations by Fox and Haskell (2001) in thick ice floes show a horizontal motion amplitude that is less than 0.1 times the vertical motion. In the absence of clear understanding of these different behaviors we test here a heuristic adjustment of the relative velocity between ice and water as a function of the floe size alone. We expect that, in general, the ice concentration, thickness, and stresses applied to the ice field also control the horizontal constraints on wave-induced motions.

For a frequency f, we reduce the contribution to the relative water-ice velocity variance $u^2(f)$ as

$$u'^2(f)=u^2(f)\left\{\frac{1}{2}\left[1+\tanh\left(\frac{D_{max}-r_D\lambda(f)}{0.5D_{max}}\right)\right]\right\}^2, \quad (6)$$

with $r_D = 0.3$ an empirically adjusted parameter and $\lambda(f)$ the wavelength of the waves of frequency f. As a result, the dissipation rate is strongly reduced for waves longer than D_{max}/r_D, and there is no reduction for maximum floe diameters of the order of the wavelength or more. The factor 0.5 D_{max} in the denominator smooths the reduction over a wide range of floe sizes.

3.2. Model Sensitivity

Model results for these different adjustments are shown in Figure 8, with all the modified parameters listed in Table 1.

With the proposed reduction in basal friction, the overall dissipation is reduced (run DBF in Figure 8). This can be compensated by an adjustment of the nonlinear inelastic flow parameter B_{ine} from 3×10^7 to 1×10^7 N m^2 s$^{1/3}$. In that case, the strongest dissipative term becomes the inelastic dissipation, and the overall attenuation becomes more sensitive to the ice thickness.

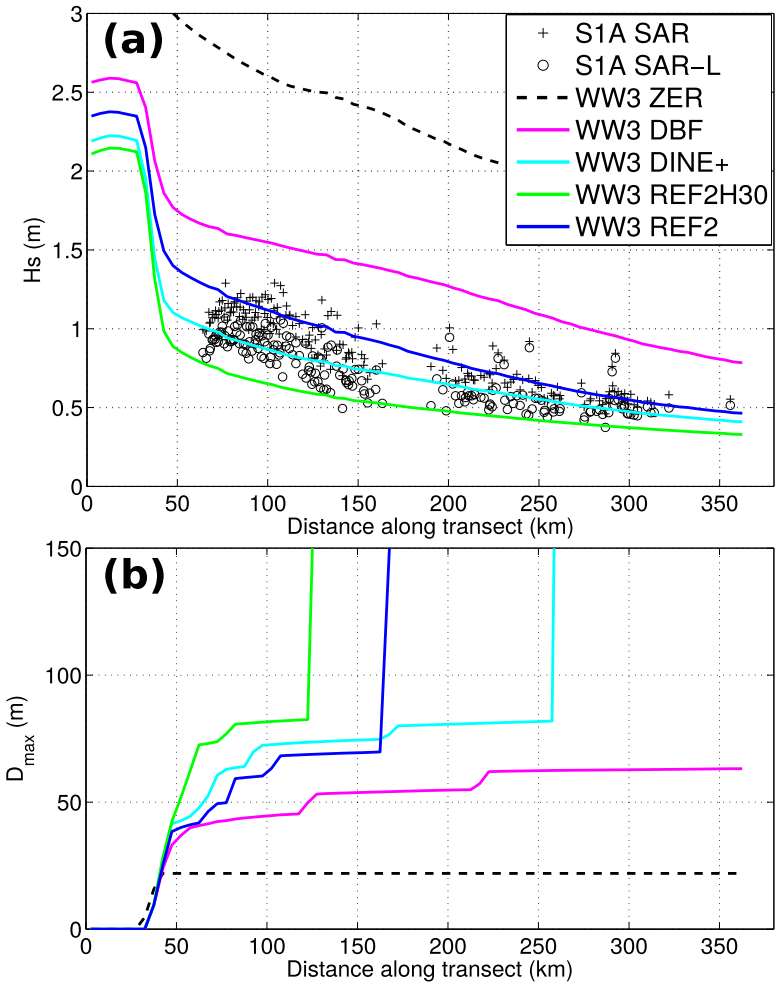

Figure 8. Same as Figure 7, but with different model runs, here using a reduced basal friction in the presence of broken ice. The AWAC-I instrument is located at $x = 135$ km. The "half broken" ice texture in the SAR image is found between 127 and 145 km.

Increasing the flexural strength from $\sigma_c = 0.274$ MPa makes it more difficult to break the ice and moves the limit of the ice breakup closer to the position of the AWAC-I mooring. Timco and O'Brien (1994) report strengths ranging from 0.2 to 1 MPa for temperatures warmer than -10°C. We note that Kohout et al. (2016) observed breakup with an estimated $\sigma_c = 0.22$ MPa using a wave height that was 0.7 H_s whereas the maximum wave height over 20 min is typically 1.8 H_s, using that value would give $\sigma_c = 0.7$ MPa. We thus make final adjustment of $\sigma_c = 0.6$ MPa, giving a "REF2" simulation that is a plausible combination of ice forcing and dissipation processes. The observations fall between the REF2 simulation, with an ice thickness $H_i = 15$ cm and the simulation with an ice thickness of 30 cm and all other parameters kept constant (REF2H30).

The resulting maps of wave heights and floe sizes for the REF2 simulations are shown in Figure 9. The position of the ice breakup front which is located 30 km from the AWAC-I mooring can be adjusted to a wide range of positions using the range of possible ice strengths given by Timco and O'Brien (1994). With our parameterizations, a shift in the ice breakup region will have a feedback effect on the wave attenuation, with smaller floes giving less attenuation and more scattering. In all cases shown here, our wave scattering parameterization contributes to changes in wave heights that are less than 0.1 m. This weak effect is consistent with the analysis by Montiel et al. (2018) for this same case.

4. Discussion

Given that we are considering the combination of three different ice interaction processes, and given the limited information on ice properties, it is not surprising that there are many ways to adjust the model forcing

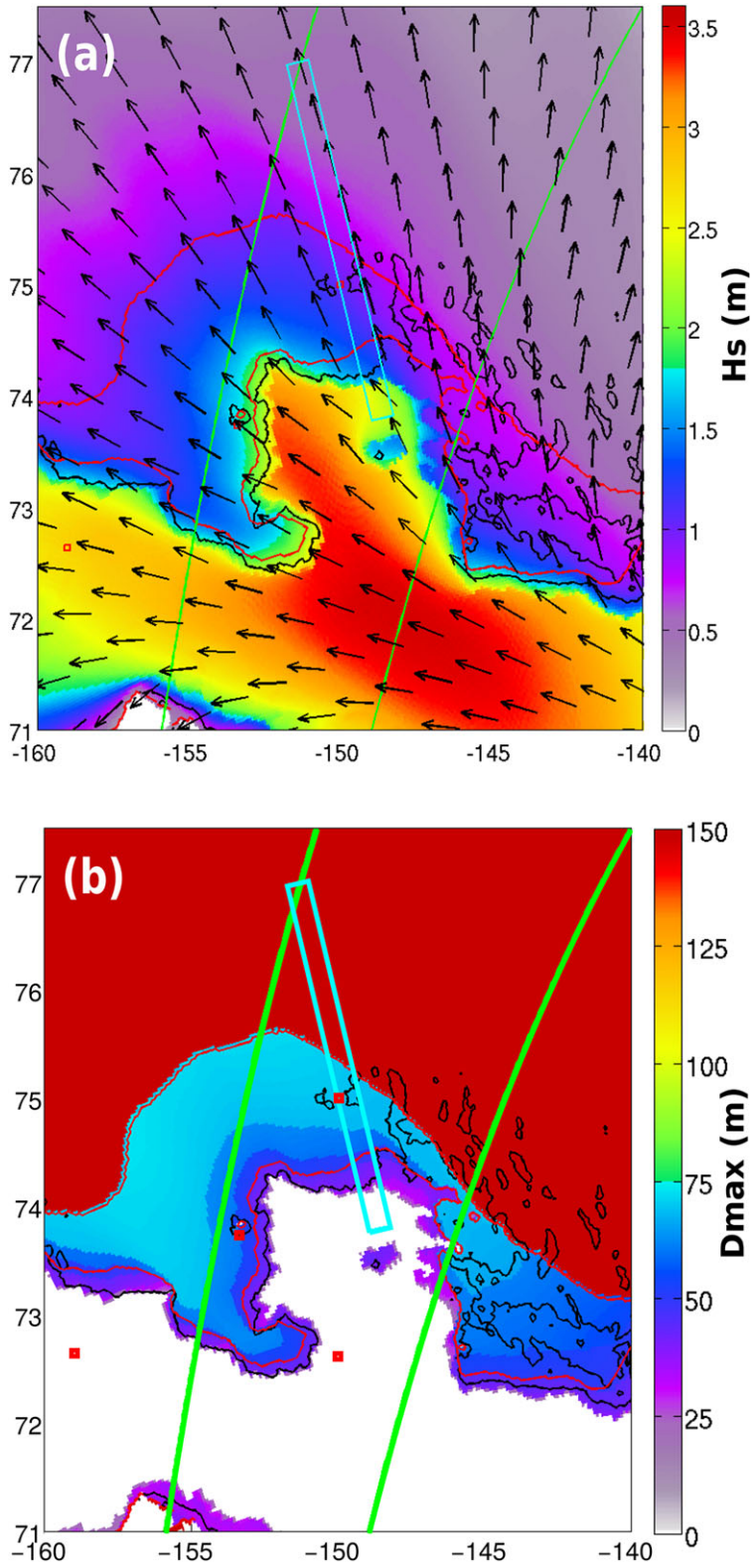

Figure 9. Modeled maps of (a) H_s and (b) D_{max} in colors for the REF2 model simulation. The black line indicating the 70% ice concentration contour, derived from AMSR2, and the red lines show the 50 and 75 m contours of D_{max}. The green lines mark the edges of the S1A swath observed on that day. In all three plots, the locations of in situ instruments are indicated by white or red squares. The cyan transect identifies the region where the wave properties are analyzed in more detail.[TQ3]

and parameters that can reproduce the main observed ice floe and wave height features. The wave attenuation is, in particular, of the same order of what was adjusted by Cheng et al. (2017) using a viscoelastic model. We have explored a possible range of ice conditions and wave-ice interaction parameters for the wave event recorded on 12 October 2015 during the "Sea State" cruise.

A more general conclusion on the applicability of this or that parameterization will require a joint analysis of many different cases, including very different frequencies, such as the $f < 0.05$ Hz waves investigated by Ardhuin et al. (2016). In addition, a larger range of sea ice conditions in the Arctic and Antarctic should be tested where observations are still sparse. Indeed the different parameterizations have very different frequency and wave amplitude dependencies. Whereas the viscoelastic model used by Cheng et al. (2017) gives variation steeper than f^8 for $f < 0.1$ Hz, basal friction is more uniform with a frequency dependency between $f^{3.5}$ and $f^{4.5}$ (Stopa et al., 2016, Figure 1), that increases by our correction for the effect of floe sizes. The nonlinear inelastic dissipation introduced by Boutin et al. (2018) has a larger f^8 dependency and, more interestingly, it has a strong dependency on the wave amplitude, with a quadratic increase of the half-decay distance for lower amplitudes. This amplitude effect could be the cause for the observed reduction in wave decay rate along the propagation path that is reported in Part 1.

5. Conclusions

In this paper, we have examined the evolution of storm waves, with dominant periods around 10 s, across the wide Marginal Ice Zone observed in the Beaufort Sea on 12 October 2015. Wave height estimations from SAR imagery have been performed up to 400 km into the ice. These data allowed us to evaluate the parameterizations presented by Boutin et al. (2018) for scattering by ice floes, basal friction, and inelastic dissipation due to dislocations in the ice and ice breakup.

From the model result, we conclude that dissipative mechanisms are dominant for the observed thin ice, in the range 0.1–0.4 m, and wave periods, around 10 s. Indeed, scattering has a weaker effect on wave heights. Our first model simulations suggested that molecular viscosity for basal friction under a continuous ice layer gives a too strong dissipation near the ice edge. We thus introduced an ad hoc reduction of basal friction for broken ice, based on the idea that the ice is able to follow part of the horizontal motion. With this adjustment, ice breakup and wave attenuation are well reproduced with a realistic combination of basal friction and flexural dissipation.

The first large scale and semiautomatic application of a wave height measurement method from SAR imagery in sea ice (Part 1) has given a unique data set for the analysis of waves evolution over large distances. The combination of Part 1 results with our present analyses clearly shows that the SAR-derived azimuthal cut-off in the ice for the Sentinel-1A IW mode is only valid near the ice edge. Further in the ice, as the wave spectrum becomes narrow, the cut-off parameter λ_c should decrease like the wave heights, but it does not. As a result, the wave height estimated in the first 30 km of the ice is not reliable because the azimuthal cut-off is still significant but it cannot be estimated from the SAR image. More frequent acquisition of IW mode data over sea ice, giving a wider range of waves and ice conditions, would certainly help to improve on the wave retrieval algorithm, and to better constrain wave-ice interaction processes.

Acknowledgments

This work was supported by the EU-FP7 project SWARP under grant agreement 607476, ONR grant N0001416WX01117, and CNES, it is based on observations with Sentinel-1 kindly provided by ESA. Visualization and analysis were greatly facilitated by the Syntool portal developed by OceanDataLab: https://swarp.oceandatalab.com. Support from LabexMer via grant ANR-10-LABX-19-01, and Copernicus Marine Environment Monitoring Service (CMEMS) as part of the Service Evolution program is gratefully acknowledged. The deployment and recovery of the northern AWAC were conducted by the NSF-funded BGOS (Beaufort Gyre Observing System) program. Data, supplemental material, and a cruise report can be found at http://www.apl.uw.edu/arcticseastate. Numerical model simulations are available at ftp://ftp.ifremer.fr/ifremer/ww3/COM/PAPERS/.

References

Ardhuin, F., Chapron, B., Collard, F., Smith, M., Stopa, J., Thomson, J., et al. (2017a). Measuring ocean waves in sea ice using SAR imagery: A quasi-deterministic approach evaluated with sentinel-1 and in situ data. *Remote Sensing of Environment*, *189*, 211–222. https://doi.org/10.1016/j.rse.2016.11.024

Ardhuin, F., Collard, F., Chapron, B., Girard-Ardhuin, F., Guitton, G., Mouche, A., et al. (2015). Estimates of ocean wave heights and attenuation in sea ice using the SAR wave mode on Sentinel-1A. *Geophysical Research Letters*, *42*, 2317–2325. https://doi.org/10.1002/2014GL062940

Ardhuin, F., Rascle, N., Chapron, B., Gula, J., Molemaker, J., Gille, S. T., et al. (2017b). Small scale currents have large effects on wind wave heights. *Journal of Geophysical Research: Oceans*, *122*, 4500–4517. https://doi.org/10.1002/2016JC012413

Ardhuin, F., Rogers, E., Babanin, A., Filipot, J.-F., Magne, R., Roland, A., et al. (2010). Semi-empirical dissipation source functions for wind-wave models: Part I, definition, calibration and validation. *Journal of Physical Oceanography*, *40*(9), 1917–1941.

Ardhuin, F., Sutherland, P., Doble, M., & Wadhams, P. (2016). Ocean waves across the Arctic: Attenuation due to dissipation dominates over scattering for periods longer than 19 s. *Geophysical Research Letters*, *43*, 5775–5783. https://doi.org/10.1002/2016GL068204

Boutin, G., Ardhuin, F., Dumont, D., Sévigny, C., & Girard-Ardhuin, F. (2018). Floe size effects on wave-ice interactions: Theoretical background, implementation and applications. *Journal of Geophysical Research: Oceans.*

Cheng, S., Rogers, W. E., Thomson, J., Smith, M., Doble, M. J., Wadhams, P., et al. (2017). Calibrating a viscoelastic sea ice model for wave propagation in the arctic fall marginal ice zone. *Journal of Geophysical Research: Oceans*, *122*, 8770–8793. https://doi.org/10.1002/2017JC013275

Cole, D. M., & Durell, G. D. (2001). A dislocation-based analysis of strain history effects in ice. *Philosophical Magazine A*, *81*(7), 1849–1872. https://doi.org/10.1080/01418610108216640

Collins, C. O. III, Rogers, W. E., Marchenko, A., & Babanin, A. V. (2015). In situ measurements of an energetic wave event in the Arctic marginal ice zone. *Geophysical Research Letters*, *42*, 1863–1870. https://doi.org/10.1002/2015GL063063

de Carolis, G., Olla, P., & Pignagnoli, L. (2005). Effective viscosity of grease ice in linearized gravity waves. *Journal of Fluid Mechanics*, *535*, 369–381. https://doi.org/10.1017/S002211200500474X

Doble, M. J., & Bidlot, J.-R. (2013). Wave buoy measurements at the Antarctic sea ice edge compared with an enhanced ECMWF WAM: Progress towards global waves-in-ice modelling. *Ocean Modelling*, *70*, 166–173. https://doi.org/10.1016/j.ocemod.2013.05.012

Fox, C., & Haskell, T. G. (2001). Ocean wave speed in the Antarctic marginal ice zone. *Annales Geophysicae*, *33*, 350–354. https://doi.org/10.3189/172756401781818239

Gelci, R., Cazalé, H., & Vassal, J. (1957). Prévision de la houle. La méthode des densités spectroangulaires. *Bulletin d'information du Comité d'Océanographie et d'Etude des Côtes*, *9*, 416–435.

Gohin, F., & Cavanié, A. (1994). A first try at identification of sea ice using the three beam scatterometer of ERS-1. *International Journal of Remote Sensing*, *15*(6), 1221–1228.

Grant, W. D., & Madsen, O. S. (1979). Combined wave and current interaction with a rough bottom. *Journal of Geophysical Research*, *84*, 1797–1808.

Guest, P., Persson, P. O. G., Wang, S., Jordan, M., Jin, Y., Blomquist, B., & Fairall, C. (2018). Low-level baroclinic jets over the new Arctic Ocean. *Journal of Geophysical Research: Oceans*, *123*. https://doi.org/10.1002/2018JC013778

Hasselmann, K., & Hasselmann, S. (1991). On the nonlinear mapping of an ocean wave spectrum into a synthetic aperture radar image spectrum and its inversion. *Journal of Geophysical Research*, *96*, 10713–10729.

Hasselmann, S., & Hasselmann, K. (1985). Computation and parameterizations of the nonlinear energy transfer in a gravity-wave spectrum. Part I: A new method for efficient computations of the exact nonlinear transfer. *Journal of Physical Oceanography*, *15*, 1369–1377.

Itkin, P., Spreen, G., Cheng, B., Doble, M., Girard-Ardhuin, F., Haapala, J., et al. (2017). Thin ice and storms: Sea ice deformation from buoy arrays deployed during n-ice2015. *Journal of Geophysical Research: Oceans*, *122*, 4661–4674. https://doi.org/10.1002/2016JC012403

Kaleschke, L., Lüpkes, C., Vihma, T., Haarpaintner, J., Hartmann, A. B. J., & Heygster, G. (2001). SSM/I sea ice remote sensing for mesoscale ocean-atmospheres. *Canadian Journal of Remote Sensing*, *27*(5), 526–537.

Kaleschke, L., Tian-Kunze, X., Maaß, N., Mkynen, M., & Drusch, M. (2012). Sea ice thickness retrieval from SMOS brightness temperatures during the arctic freeze-up period. *Geophysical Research Letters*, *39*, L05501. https://doi.org/10.1029/2012GL050916

Kerbaol, V., Chapron, B., & Vachon, P. (1998). Analysis of ERS-1/2 synthetic aperture radar wave mode imagettes. *Journal of Geophysical Research*, *103*, 7833–7846.

Kohout, A. L., & Meylan, M. H. (2008). An elastic plate model for wave attenuation and ice floe breaking in the marginal ice zone. *Journal of Geophysical Research*, *113*, C09016. https://doi.org/10.1029/2007JC004434

Kohout, A. L., Williams, M. J. M., Dean, S. M., & Meylan, M. H. (2014). Storm-induced sea-ice breakup and the implications for ice extent. *Nature*, *509*, 604–607. https://doi.org/10.1038/nature13262

Kohout, A., Williams, M. J. M., Toyota, T., Lieser, J., & Hutchings, J. (2016). In situ observations of wave-induced sea ice breakup. *Deep-Sea Research, Part II*, *131*, 22–27. https://doi.org/10.1016/j.dsr2.2015.06.010

Liu, A. K., Holt, B., & Vachon, P. W. (1991). Wave propagation in the marginal ice zone' model predictions and comparisons with buoy and synthetic aperture radar data. *Journal of Geophysical Research*, *96*, 4605–4621.

Liu, A. K., & Mollo-Christensen, E. (1988). Wave propagation in a solid ice pack. *Journal of Physical Oceanography*, *18*, 1702–1712.

Lund, B., Graber, H. C., Persson, P. O. G., Smith, M., Doble, M., Thomson, J., et al. (2018). Arctic sea ice drift measured by shipboard marine radar. *Journal of Geophysical Research: Oceans*, *123*, 4298–4321. https://doi.org/10.1029/2018JC013769

Madsen, O. S. (1994). Spectral wave-current bottom boundary layer flows. In *Proceedings of the 24th international conference on coastal engineering* (pp. 384–397). Reston, VA: American Society of Civil Engineers.

Manucharyan, G. E., & Thompson, A. F. (2018). Submesoscale sea ice-ocean interactions in marginal ice zones. *Journal of Geophysical Research: Oceans*, *122*, 9455–9475. https://doi.org/10.1002/2017JC012895

Marchenko, A. V., & Chumakov, M. M. (2017). Study the surface gravity waves damping in the marginal ice zone of drifting ice in the Barents Sea. In Mansurov, M. N. & Onishchenko, D. A. (Eds.), *Modern approach and promising technologies within the projects for development of oil and gas fields at Russian continental shelf* (Vol. 32pp. 94–103). Gazprom: Vesti Gazovoy Nauki.

Masson, D. (1991). Wave-induced drift force in the marginal ice zone. *Journal of Physical Oceanography*, *21*(7), 3–10.

Montiel, F., Squire, V. A., Doble, M., Thomson, J., & Wadhams, P. (2018). Attenuation and directional spreading of ocean waves during a storm event in the autumn Beaufort Sea marginal ice zone. *Journal of Geophysical Research: Oceans*. https://doi.org/10.1029/2018JC013763

Mosig, J. E. M., Montiel, F., & Squire, V. A. (2015). Comparison of viscoelastic-type models for ocean wave attenuation in ice-covered seas. *Journal of Geophysical Research: Oceans*, *120*, 6072–6090. https://doi.org/10.1002/2015JC010881

Nye, J. F. (1953). The flow law of ice from measurements in glacier tunnels, laboratory experiments and the Jungfraufirn borehole experiment. *Proceedings of the Royal Society of London. Series A*, *219*(1139), 477–489.

Pickart, R. S. (2004). Shelfbreak circulation in the Alaskan Beaufort Sea: Mean structure and variability. *Journal of Geophysical Research*, *109*, C04024. https://doi.org/10.1029/2003JC001912

Rascle, N., & Ardhuin, F. (2013). A global wave parameter database for geophysical applications. Part 2: Model validation with improved source term parameterization. *Ocean Modelling*, *70*, 174–188. https://doi.org/10.1016/j.ocemod.2012.12.001

Rogers, W. E., & Campbell, T. J. (2009). *Implementation of curvilinear coordinate system in the WAVEWATCH III model* (Memorandum Rep. NRL/MR/7320-09-9193, 42 p.). Washington, DC: Naval Research Laboratory.

Rogers, W. E., Thomson, J., Shen, H. H., Doble, M. J., Wadhams, P., & Cheng, S. (2016). Dissipation of wind waves by pancake and frazil ice in the autumn Beaufort Sea. *Journal of Geophysical Research: Oceans*, *121*, 7991–8007. https://doi.org/10.1002/2016JC012251

Spreen, G., Kaleschke, L., & Heygster, G. (2008). Sea ice remote sensing using AMSR-E 89-GHz. *Journal of Geophysical Research*, *113*, C02S03. https://doi.org/10.1029/2005JC003384

Squire, V., Dugan, J., Wadhams, P., Rottier, P., & Liu, A. (1995). Of ocean waves and sea ice. *Annual Review of Fluid Mechanics*, *27*(3), 115–168.

Stopa, J. E., Ardhuin, F., Thomson, J., Smith, M. M., Kohout, A., Doble, M., & Wadhams, P. (2018), Wave attenuation through an Arctic Marginal Ice Zone on 12 October 2015: 1. Measurement of wave spectra and ice features from Sentinel-1A. *Journal of Geophysical Research*, *123*, 3619–3634. https://doi.org/10.1029/2018JC013791

Stopa, J. E., Ardhuin, F., Chapron, B., & Collard, F. (2015). Estimating wave orbital velocity through the azimuth cutoff from space-borne satellite. *Journal of Geophysical Research: Oceans*, *130*, 7616–7634. https://doi.org/10.1002/2015JC011275

Stopa, J. E., Ardhuin, F., Husson, R., Jiang, H., Chapron, B., & Collard, F. (2016). Swell dissipation from 10 years of Envisat ASAR in wave mode. *Geophysical Research Letters*, *43*, 3423–3430. https://doi.org/10.1002/2015GL067566

Stopa, J. E., Sutherland, P., & Ardhuin, F. (2018). Strong and highly variable push of ocean waves on southern ocean sea ice. *Proceedings of the National Academy of Sciences of the United States of America*, *115*, 5861–5865. https://doi.org/10.1073/pnas.1802011115

Sutherland, P., & Gascard, J. C. (2016). Airborne remote sensing of ocean wave directional wavenumber spectra in the marginal ice zone. *Geophysical Research Letters*, *43*, 4659–4664. https://doi.org/10.1002/grl.53444

The WAVEWATCH III® Development Group (2016). *User manual and system documentation of WAVEWATCH III® version 5.16* (Tech. Note 329, 326 p. + Appendices). College Park, MD: NOAA/NWS/NCEP/MMAB.

Thomson, J., Ackley, S., Girard-Ardhuin, F., Ardhuin, F., Babanin, A., Boutin, G., et al. (2018). Overview of the arctic sea state and boundary layer physics program. *Journal of Geophysical Research*. https://doi.org/10.1002/2018JC013766

Thomson, J., Ackley, S., Shen, H. H., & Rogers, W. E. (2017). The balance of ice, waves, and winds in the arctic autumn. *Eos Transactions American Geophysical Union*, *98*, https://doi.org/10.1029/2017EO066029

Timco, G. W., & O'brien, S. (1994). Flexural strength equation for sea ice. *Cold Regions Science and Technology*, *22*, 285–298.

Wadhams, P. (1973). Attenuation of swell by sea ice. *Journal of Geophysical Research*, *78*, 3552–3563.

Wadhams, P., & Doble, M. J. (2009). Sea ice thickness measurement using episodic infragravity waves from distant storms. *Cold Regions Science and Technology*, *56*, 98–101. https://doi.org/10.1016/j.coldregions.2008.12.002

Wadhams, P., Squire, V. A., Ewing, J. A., & Pascal, R. W. (1986). The effect of the marginal ice zone on the directional wave spectrum of the ocean. *Journal of Physical Oceanography*, *16*, 358–376.

Wamdi Group (1988). The WAM model—A third generation ocean wave prediction model. *Journal of Physical Oceanography*, *18*, 1775–1810.

Williams, T. D., Bennetts, L. G., Squire, V. A., Dumont, D., & Bertino, L. (2013). Wave-ice interactions in the marginal ice zone. Part 1: Theoretical foundations. *Ocean Modelling*, *70*, 81–91. https://doi.org/10.1016/j.ocemod.2013.05.010

Zhao, X., & Shen, H. H. (2015). Wave propagation in frazil/pancake, pancake, and fragmented ice covers. *Cold Regions Science Technology*, *113*, 71–80. https://doi.org/10.1016/j.coldregions.2015.02.007